Journal of Inorganic and General Chemistry
ZAAC
Zeitschrift für anorganische und allgemeine Chemie
www.zaac.wiley-vch.de
REVIEW

DOI: 10.1002/zaac.202300109

Special Collection

Laves phases: superstructures induced by coloring and distortions

Elias C. J. Gießelmann,[a] Rainer Pöttgen,*[b] and Oliver Janka*[a]

In recognition of the outstanding scientific achievements by Eduard Zintl on the occasion of his 125th birthday

The structural chemistry of Laves phases, especially with respect to their superstructures induced by coloring and distortions is discussed. Starting from the three classical Laves phases $MgCu_2$, $MgZn_2$ and $MgNi_2$, the more complex Komura phases are derived. Different possibilities of their description are summarized. In the second part, the superstructures are discussed based on their respective prototypes. The crystal chemical relationships are illustrated based on group-subgroup descriptions using the Bärnighausen formalism.

1. Introduction

Laves phases, named after *Fritz H. Laves*,[1,2] a German mineralogist, are an important class of compounds, both from a structural and property point of view. In the case of the binary compounds, they exhibit the general composition AB_2. Three prototypes are known: cubic $MgCu_2$ (C15, $Fd\bar{3}m$),[3] and the two hexagonal variants $MgZn_2$ (C14)[4,5] and $MgNi_2$ (C36)[6,7] (both space group type $P6_3/mmc$).[8] Based on the similarities in their crystal structures, Schulze suggested to name compounds adopting one of these structures "Laves phases".[9] In 2006, a special issue was published on the occasion of Laves' 100th birthday (*Z. Kristallogr.* **2006**, *221*, issues 5–7) including eulogies on Laves work[1,2,10] and summarizing different aspects of the work on Laves phases.[11–15]

One can distinguish between three different important aspects in the field of Laves phase research: (1) The structural aspects including the formation of superstructures and coloring variants, (2) the assessment of the stability of the different structure types and, closely connected, the analysis of the chemical bonding and finally (3) the physical properties of Laves phases.

With respect to the bonding aspect, the works of Ormeci, Simon and Grin on the "Structural topology and chemical bonding in Laves phases",[16] the work of Johnston and Hoffmann on "Structure-bonding relationships in the Laves Phases"[17] and Nesper on "Bonding patterns in intermetallic compounds"[18,19] have to be mentioned. Also, the two articles of Stein, Palm and Sauthoff addressing "Structure and stability of Laves phases"[20,21] discuss important aspects of this question.

With respect to the properties, the review of Stein and Leineweber on the functional and structural applications of Laves phases,[22] the work of Gschneidner Jr., Pecharsky and Tsokol on magnetocaloric materials[23] as well as the work of Yartys and Lototskyy or Matar on Laves phases as hydrogen storage materials should be noted.[24,25] Furthermore, the reviews on Laves phases for Ni/MH battery applications[26] and the review on the high-pressure crystal chemistry of intermetallics, including Laves phases[27] shall be introduced.

The relationship between the different binary Laves phase prototypes and a number of superstructures have been described by Parthé in his two handbooks,[28,29] a general guide to coloring, distortions, and puckering of intermetallics can be found in a review.[30]

As of today, the *Pearson Crystal Data Base*[31] lists over three thousand entries for binary compounds adopting these three structure types. However, also in block polymers[32] and micellar structures,[33] the structural arrangements occuring in Laves phases have been observed. This underlines the importance of the Laves phases.

This review describes the structural and crystal chemistry of Laves phases with a special focus on superstructure formation. Therefore, articles investigating properties and bonding,

[a] *E. C. J. Gießelmann, PD Dr. O. Janka*
Anorganische Festkörperchemie
Universität des Saarlandes, Campus C4.1
66123 Saarbrücken, Germany
Fax: +49-681-302-70652
E-mail: oliver.janka@uni-saarland.de
[b] *Prof. Dr. R. Pöttgen*
Institut für Anorganische und Analytische Chemie
Universität Münster
Corrensstrasse 30
48149 Münster, Germany
Fax: +49-251-83-36002
E-mail: pottgen@uni-muenster.de

Supporting information for this article is available on the WWW under https://doi.org/10.1002/zaac.202300109

This article is part of a Special Collection to celebrate Professor Eduard Zintl on the occasion of his 125th anniversary. Please see our homepage for more articles in the collection.

although being crucial for the understanding of these compounds, are not summarized encompassing in this work.

2. The binary Laves phases

Laves phases can be understood as tetrahedrally closest-packed binary structures AB_2, in which the larger *A* atoms reside within cavities of a network formed by the smaller *B* atoms. The *B* atoms arrange as empty B_4 tetrahedra which are connected in different ways. Three prototypes are known: cubic $MgCu_2$ (C15, $Fd\bar{3}m$),[3] and the two hexagonal variants $MgZn_2$ (C14)[4,5] and $MgNi_2$ (C36)[6,7] (both space group type $P6_3/mmc$).[8] In all three prototypes, both atoms exhibit large coordination numbers with CN(*A*) = 16 (4 *A* + 12 *B*) in the shape of a 16-vertex Frank-Kasper polyhedron and CN(*B*) = 12 (6 *A* + 6 *B*) in the shape of an icosahedron, respectively. For closest-packed structures, the ideal atomic radii ratio from a geometrical point of view is $r_A/r_B = (3/2)^{1/2} \approx 1.225$. This factor is realized for quite a number of compounds, however, also deviating ratios ranging from ~1.1 up to ~1.7 have been reported.[31] Given the closest-packed structure, these phases are often considered to be stabilized by packing effects.[11] This can be nicely illustrated by the fact that $NeHe_2$[34] and $Ar(H_2)_2$[35] adopt the $MgZn_2$ type structure at high pressures while $Xe(N_2)_2$ crystallizes in the cubic $MgCu_2$ type at 150 GPa.[36] Despite the geometric influences, that seem to be a dominating factor, the electronic contributions on the formation of Laves phases have already been addressed and studied numerous times.[16,17,20,21,37–39] Laves himself discussed the influence of the valence electron configuration (VEC) on the formation of these compounds in one of his early works.[8]

In the following paragraphs, different ways to understand and to visualize Laves phases will be described. The unit cells of the three binary prototypes, cubic $MgCu_2$ ($Fd\bar{3}m$, C15; Mg on 8*b*; Cu on 16*c*) as well as the hexagonal $MgZn_2$ ($P6_3/mmc$, C14; Mg on 4*f*; Zn1 on 6*h*; Zn2 on 2*a*) and $MgNi_2$ ($P6_3/mmc$, C36; Mg1 on 4*f*; Mg2 on 4*e*; Ni1 on 6*h*; Ni2 on 6*g*; Ni3 on 4*f*) type structures, are shown in Figure 1. As mentioned before, the *B* atoms in all Laves phases form empty B_4 tetrahedra. While in the cubic $MgCu_2$ type structure, these tetrahedra are connected via all corners to four other tetrahedra, in the hexagonal $MgZn_2$ phase, two tetrahedra are connected by a common face, forming an (empty) trigonal bipyramid. This entity is connected to five other entities over all corners. Finally, in the $MgNi_2$ type structure both connection modes are observed. Therefore, the latter structure type can be understood as an intergrowth between $MgCu_2$ and $MgZn_2$. In all three parent structures, the Mg atoms are located in large cavities formed by the B_4 tetrahedra network and exhibit atomic arrangements, when focused only on the Mg substructure, that are comparable to the diamond type structures. In $MgCu_2$ the arrangement of the cubic diamond is realized while in $MgZn_2$ a lonsdaleite like arrangement is observed. In $MgNi_2$, again an intergrowth of cubic and hexagonal motifs can be observed.

Instead of describing the Laves phases based on the topology of their *A* and *B* atom connectivity, the structures can be visualized based on layers or differently stacked slabs. Three different layers can be identified in the Laves phases that are stacked to form one slab.[40] These layers are: a kagome net (Figure 2, Schläfli symbol 3.6.3.6) formed by the *B* atoms as well as two different triangular nets (3^6) formed by the *A* and *B* atoms (Figure 2).[41] The construction of one slab from the different nets was described by Frank and Kasper[40] and is illustrated in Figure 2. The stacking sequence is kagome *A* (*z* =

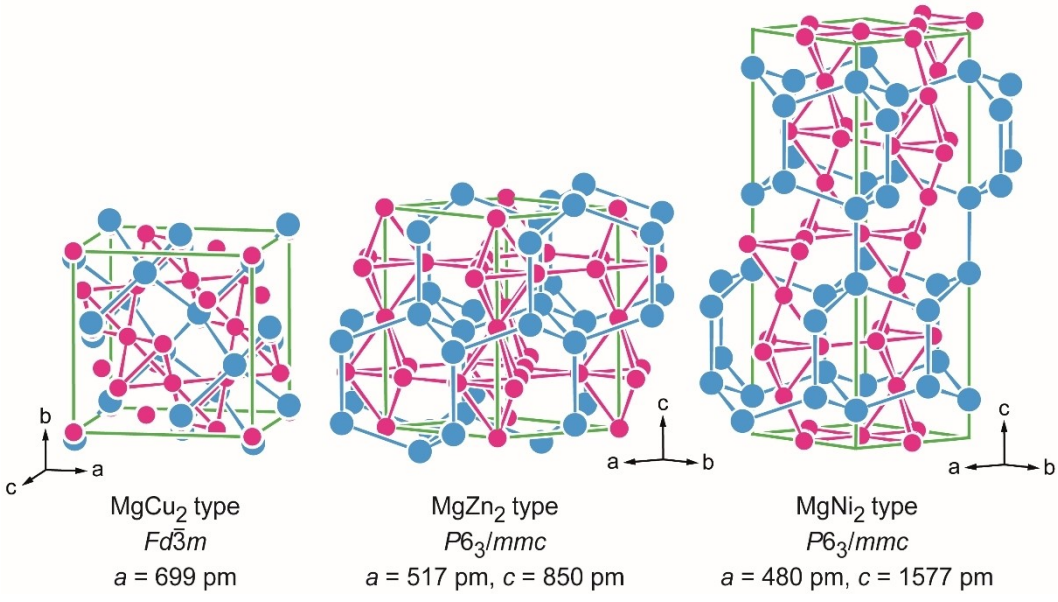

Figure 1. Unit cells of the three different binary Laves phases. The Mg atoms are drawn in blue, the transition metals Cu, Zn and Ni in magenta. Unit cell edges are highlighted in green. In addition, the space groups and lattice parameters are given.

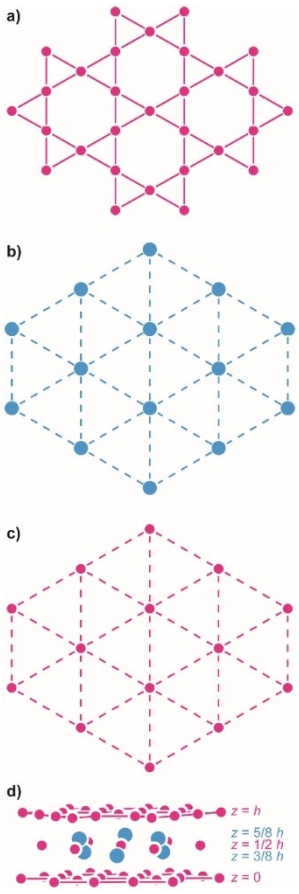

Figure 2. Layers in the Laves phases. a) kagome net formed by the *B* atoms (magenta), b) triangular nets formed by the b) *A* (blue) and c) *B* atoms. The stacking to form a slab is shown in d).

0), 3^6 *B* ($z = 3/8\ h$), 3^6 *A* ($z = 1/2\ h$), 3^6 *B* ($z = 5/8\ h$), kagome *A* ($z = h$). Alternatively, according to the description of Samson[42] one can create these slabs by using B_4 tetrahedra and B_{12} truncated tetrahedra (Figure 3, *top left*).

In the cubic Laves phase $MgCu_2$ ($Fd\bar{3}m$) only one layer type (Figure 3, *bottom left*) exists that gets stacked along the space diagonal. The slabs get stacked in an …ABC… sequence, like in the cubic closest packing and therefore one can symbolize this stacking sequence with $(\boldsymbol{c})_3$ when applying the Jagodzinski notation.[29] Alternatively, the Ramsdell notation can be used.[43] Here, the $MgCu_2$ type structure is labeled as 3C, resembling three slabs within the unit cell and a cubic stacking of these. A comparison of the different notations is given in Table 1. When looking at $MgZn_2$ and $MgNi_2$ (both space group type $P6_3/mmc$), two blocks that are identical in composition, however, mirrored to each other can be utilized for the description of the structure. Here, Jagodzinski symbols of $(\boldsymbol{h})_2$ and $(\boldsymbol{hc})_2$ arise in line with stacking sequences of …AB… and …ABAC…, respectively. The Ramsdell notation is 2H for $MgZn_2$ and 4H for $MgNi_2$, respectively. The colorations that arise from this description are shown in Figure 3.

The concept of stacking this slab[29] along with the idea of chemical twinning[44–46] can readily be used to describe even more complex Laves phases like the Komura phases.[47–54] $MgNi_{0.9}Cu_{1.1}$ ($P6_3/mmc$)[51] (Figure 4, *middle*) for example exhibits a stacking sequence of $(\boldsymbol{hcc})_2$ (Ramsdell 6H) and two mirror planes duplicating the respective blocks. In addition, the unit cells of $MgCu_{1.07}Al_{0.93}$ ($P\bar{6}m2$, Ramsdell 6H)[55] and $MgCu_{0.08}Zn_{1.92}$ ($P6_3/mmc$, 8H)[49] are shown. For both, the concept of slabs and mirror planes can be used to describe the stacking in these relatively large unit cells. The Laves phase $MgCu_{1.07}Al_{0.93}$ ($P6_3/mmc$, Ramsdell 16H) for example exhibits 16 slabs per unit cell resulting in a *c*-axis lattice parameter of ~6670 pm.[56]

Taking these descriptions and considerations into account, the Laves phases can be grouped based on the percentage of the hexagonal stacking contribution. For quite a number of examples it was observed that this contribution correlates with the VEC. The crystal chemical principles along with considerations regarding the bonding peculiarities are summarized in different original articles and reviews.[11,16–18,20,21,37,47,51,54,57–64]

When looking at the entries in the Pearson database[31] it becomes evident that the cubic and hexagonal Laves phases play a crucial role in the structural chemistry of binary intermetallic compounds. Figures 5–7 show the occurrence of all elements which are reported to be part of a binary Laves phase. The color code here depicts, whether the element is found on the *A* or *B* site. Mixed coloring means that the element is reported to be both.

For all three structure types a clear trend throughout the periodic table of elements is observed. Late transition metals are usually the network building element (Cu, Zn or Ni position), while the early transition metals and the rare earth elements are more often found to be on the Mg site. Some exceptions here are the light elements of the groups, such as Li, Be, Mg or Ti which are also found on the *B* site. In an analogous way some examples are reported, where the noble transition metals are reported to be the *A* metal.

For the cubic $MgCu_2$ type (Figure 5) almost every transition metal, all alkali and alkaline earth metals as well as all common lanthanides and actinides appear in intermetallic compounds.

Table 1. Different notations for the description of Laves phases.

Composition	space group	Strukturbericht	Pearson	Ramsdell	Jagodzinski
$MgZn_2$	$P6_3/mmc$	C14	*hP*12	2H	$(\boldsymbol{h})_2$
$MgCu_2$	$Fd\bar{3}m$	C15	*cF*24	3C	$(\boldsymbol{c})_3$
$MgNi_2$	$P6_3/mmc$	C36	*hP*24	4H	$(\boldsymbol{hc})_2$
$MgCu_{1.07}Al_{0.93}$	$P\bar{6}m2$	–	*hP*36	6H	**hchhhc**
$MgNi_{0.9}Cu_{1.1}$	$P6_3/mmc$	–	*hP*36	6H	$(\boldsymbol{hcc})_2$
$MgCu_{0.08}Zn_{1.92}$	$P6_3/mmc$	–	*hP*48	8H	$(\boldsymbol{hhhc})_2$

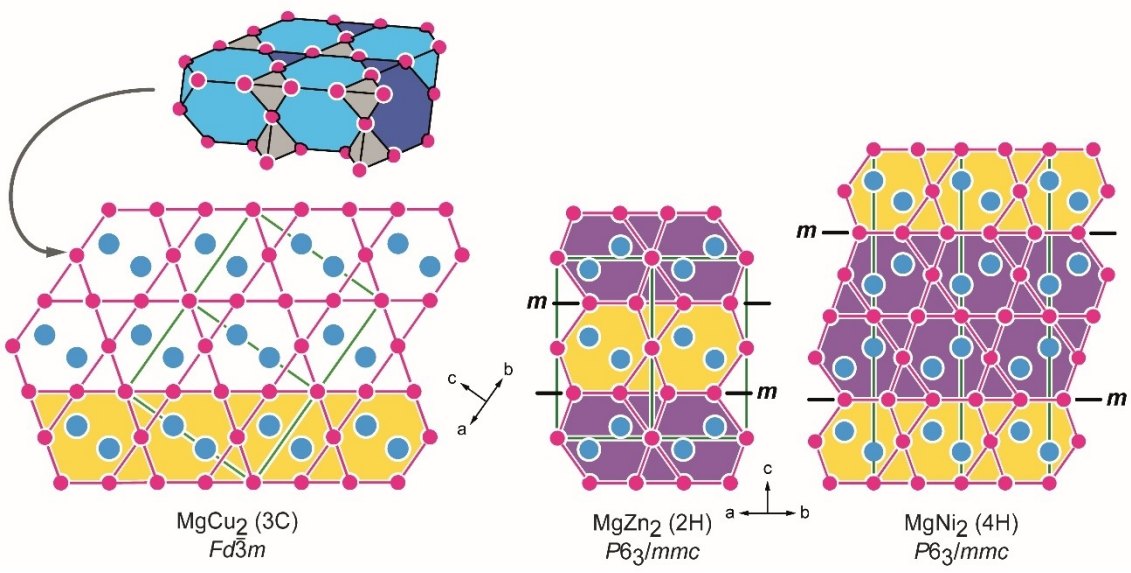

Figure 3. (*top left*) Representation of a cut out of a slab formed by B_4 tetrahedra and truncated tetrahedra B_{12}. (*bottom*) Projections of the unit cells of the Laves phases $MgCu_2$ (*left*), $MgZn_2$ (*middle*), and $MgNi_2$ (*right*). The transition metal networks formed by Cu, Zn and Ni are drawn in magenta, the magnesium atoms in blue. The blocks that derive from the $MgCu_2$ type are shaded in yellow, their mirrored versions in purple. The mirror planes (*m*) located at $z = 1/4$ and 3/4 in $MgZn_2$ and $MgNi_2$ are indicated. The unit cell edges are shown in green; the space groups are given.

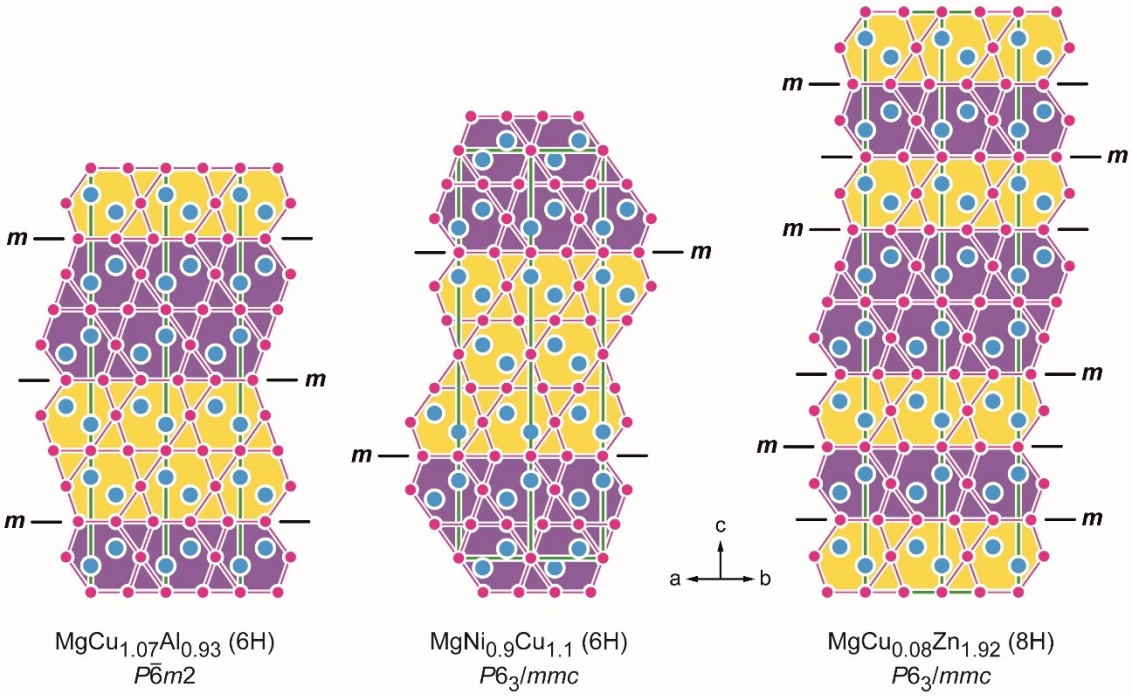

Figure 4. Projections of the unit cells of the Laves phases $MgCu_{1.07}Al_{0.93}$ (*left*), $MgNi_{0.9}Cu_{1.1}$ (*middle*), and $MgCu_{0.08}Zn_{1.92}$ (*right*). The transition metal networks (mixed occupied sites) are drawn in magenta, the magnesium atoms in blue. The blocks that derive from the $MgCu_2$ type are shaded in yellow, their mirrored versions in purple. The mirror planes (*m*) that allow the chemical twinning are indicated. The unit cell edges are shown in green; the space groups are given.

One interesting aspect emerges when looking at the Laves phases MPt_2, MCo_2, MNi_2 or MFe_2. Here, representatives of almost all metals are known. The same is true for the compounds of the main group element aluminum. It is also

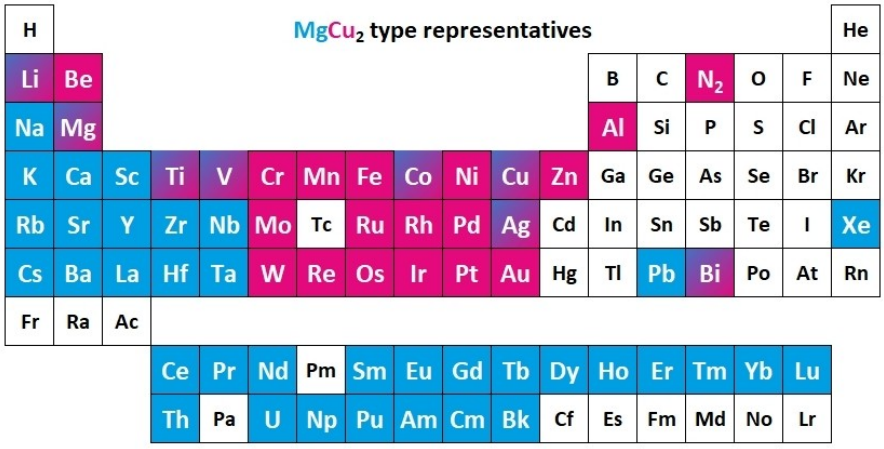

Figure 5. Compiled data from the Pearson database[31] of all elemental combinations forming the cubic $MgCu_2$ type structure. Atoms occupying the Mg positions are shown in blue, atoms forming the polyanion (Cu substructure) are highlighted in magenta. Two colored elements can occupy both sites. Note that N_2 is the building group in the respective Laves phase.

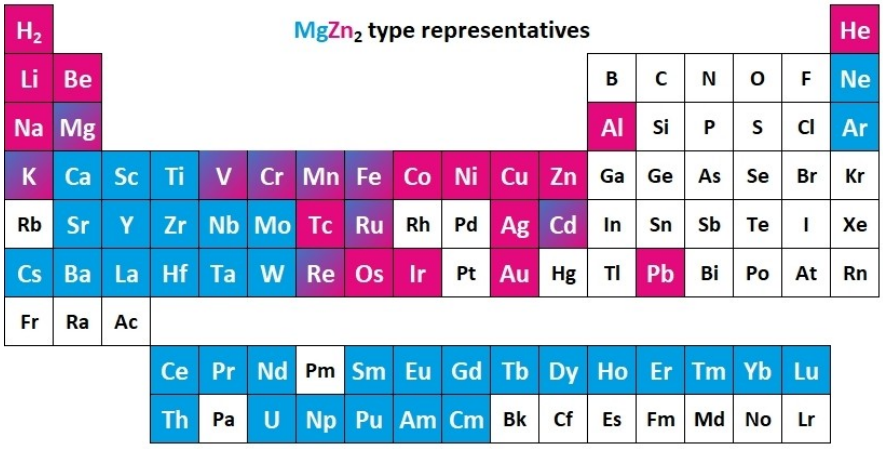

Figure 6. Compiled data from the Pearson database[31] of all elemental combinations forming the hexagonal $MgZn_2$ type structure. Atoms occupying the Mg positions are shown in blue, atoms forming the polyanion (Zn substructure) are highlighted in magenta. Two colored elements can occupy both sites. Note that H_2 is the building group in the respective Laves phase.

interesting to note, that almost no main group metal forms Laves phases with Al being the prominent exception. Here over 400 entries are listed in the Pearson database.[31] In contrast, for the other main group metals Bi and Pb only one or two combinations have been reported. All other main group elements exhibiting a somewhat metallic character such as In, Ga, Sb, Tl, are not found in any binary compounds. It becomes even more puzzling, since for example Ga is very often found in ternary ordered Laves phases (*vide infra*).

The overview for the compounds adopting the hexagonal $MgZn_2$ type structure is shown in Figure 6. It is comparable to the one for $MgCu_2$. The rather electron poor elements act as *A* atoms (with the exception of the light alkali metals) while the more electron rich elements occupy the *B* site. Exceptions can be found in the central part of the transition metals.

For the $MgNi_2$ type (Figure 7) it becomes clear, that this more complex structure type is not that often found, but again the same trend as for $MgCu_2$ and $MgZn_2$ is also observed here.

Taking a closer look at the existence ranges for some element combinations (Figure 5–7), one can see, that all three structure types are reported. In the following, one example where all three Laves phase structures are observed will be used to illustrate the occurance on this trimorphism. For the general system MCr_2 the Pearson database reveals that this composition exists for the metals of group 4 and 5. Figure 8 depicts the reported occurrence for the three Laves phases in this system. For the group 4 elements (Ti, Zr, Hf) and Ta all three structures are found in the system MCr_2 depending on different pathways in the synthesis.

The investigations on the polymorphism of $TiCr_2$ and $ZrCr_2$ will therefore be briefly discussed in the following paragraph. For $ZrCr_2$ it was found that the occurrence of the polymorphism

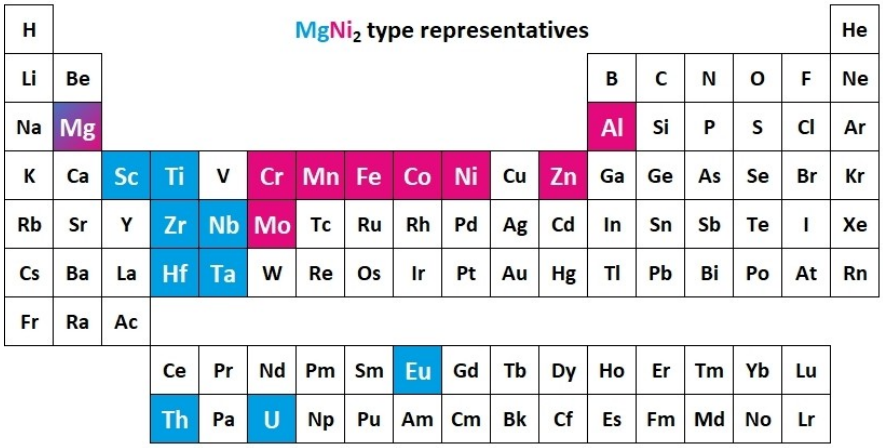

Figure 7. Compiled data from the Pearson database[31] of all elemental combinations forming the hexagonal $MgNi_2$ type structure. Atoms occupying the Mg positions are shown in blue, atoms forming the polyanion (Ni substructure) are highlighted in magenta. Two colored elements can occupy both sites.

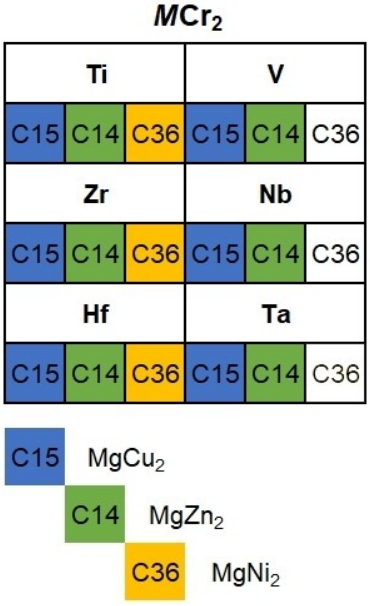

Figure 8. Existence ranges for the three different Laves phase structure types for several MCr_2 compounds.

and the existence range of the structure types mainly depends on the temperature treatment and the composition of the received material.[65] The formation of the different phases depends on the solubility ranges of the intermetallic phases with respect to the metals. It is reported that for as-cast samples with the nominal composition $ZrCr_2$ the received sample is inhomogeneous, whereas all three modifications can be observed. However, the two hexagonal structure types ($MgZn_2$ and $MgNi_2$ type) are way more prominent. It is further discussed, that the cubic Laves phase is obtained phase pure when annealing the sample at 1540 K. It is concluded that the hexagonal structures (mixture of C15 and C36) are the high temperature phases which are obtained in high amounts when quenching the sample after arc-melting is applied. The cubic phase is obtained phase pure when annealing the sample below the melting point, making it the room temperature phase. The differences in the composition within the individual structures can furthermore be illustrated by the different specific volumes (V/Z). For $ZrCr_2$, values of $V/Z = 46.79$ Å^3 ($MgCu_2$ type), 46.81 Å^3 ($MgZn_2$ type) and 48.86 Å^3 ($MgNi_2$ type) are obtained.[65] One can clearly see that the cubic structure exhibits the smallest specific volume due to the highest degree of ordering while the hexagonal phases show larger volumes in line with the formation of partial solid solutions.

For $TiCr_2$ basically the same results are observed with the cubic Laves phase being the room temperature phase and the hexagonal structures the high temperature phases.[66–69] Here it is reported that the transition temperatures strongly depend on the nominal composition of the material whereas the compounds allow a certain solubility of either titanium or chromium in the structures. Baumann and Leineweber[69] reported that the formation of the more complex $MgNi_2$ type for $TiCr_2$ can be attributed to "anti-site occupation", meaning that Ti atoms partially occupy the Cr positions. Through this study the occurrence of vacancies which create solid solubility and define the existence ranges of the certain structures could be excluded. This is also recognizable in the V/Z values ($V/Z =$ 41.80 Å^3 for the $MgCu_2$ type, 41.68 Å^3 for the $MgZn_2$ type, 41.68 Å^3 for the $MgNi_2$ type).[70]

The general process of these phase transitions (C14–C15–C36) is described in literature as well.[71] It is commonly accepted that the transition is caused by shear transformations based on the concept of synchro shear.[72]

Finally, the $AEAl_2$ (AE = Ca, Sr and Ba) phases should be mentioned. Here, $CaAl_2$ forms the cubic Laves phase,[73] however, $SrAl_2$[74] crystallizes in the orthorhombic KHg_2 type[75] structure (*Imma*), while $BaAl_2$, although initially reported to be existent, had to be revised to be Ba_7Al_{13} ($P\bar{3}m1$).[76,77] Reinvestigations of Ba_7Al_{13} by selected area and convergent beam electron diffraction in a

TEM revealed a superstructure with space group $P31m$ and a composition of $Ba_{21}Al_{40}$.[78] However, $SrAl_2$, Ba_7A_{13} and $Ba_{21}Al_{40}$ can be transformed into the cubic $MgCu_2$ type structure using high-pressure / high-temperature techniques.[79–82]

3. Ternary Laves phases – coloring variants

3.1. Coloring variants of $MgCu_2$

In this chapter, the possibility for the formation of ternary Laves phases by coloration of the polyanion will be discussed. As the cubic $MgCu_2$ type structure only exhibits two crystallographic positions, one for the Mg and one for the Cu atoms, a coloration of the Cu network is only possible when the space group symmetry is reduced. This will be discussed in chapter 4. Therefore, no coloring variants for $MgCu_2$ are possible.

3.2. Coloring variants of $MgZn_2$

The hexagonal $MgZn_2$ type structure in contrast has two Zn positions (2*a* and 6*h*) which allows for a coloration of these two sites. Therefore, two general formulae can be deduced: M_2TX_3 and M_2T_3X. The prominent prototype for the latter coloring variant is the Mg_2Cu_3Si type[83,84] with space group $P6_3/mmc$. The Pearson database[31] lists 51 entries that are directly assigned to this structure type. However, an additional over 1000 entries are given for ternary compounds adopting the $MgZn_2$ type structure. Here, the question arises whether the latter compounds are assigned correctly. For this, one has to differentiate between fully ordered compounds and those that exhibit solid solutions with mixing of atoms onto the 2*a* and 6*h* site. While some compounds have been reported to adapt the Mg_2Cu_3Si type structure, others have been assigned to this structure type despite the fact that small amounts of mixing have been determined by single crystal X-ray diffraction (e.g. Ce_2RuAl_3[85]).

Despite the discussion about the prototype, interesting aspects can be observed from the reported compounds. For example, the aluminum containing compounds almost exclusively exhibit the M_2TAl_3 composition (e.g. the RE_2TAl_3 series[86]), however, due to the formation of solid solutions, they can also be described as $MT_{0.5}Al_{1.5}$ members. For Si in contrast, rather the M_2T_3Si composition is observed, for example for the $(Sc,Ti)_2M_3Si$ (M = Cr, Mn, Fe, Co, Ni) series.[87] Again, mixing of the M and Si is observed making $MT_{1.5}Si_{0.5}$ the more appropriate description.

The flexibility of this structure type can be demonstrated as also equiatomic compounds have been reported to adopt the $MgZn_2$ type structure and also various other solid solutions.[14,15,88–92]

3.3. Coloring variants of $MgNi_2$

When searching the Pearson database[31] for ternary ordering variants of the hexagonal $MgNi_2$ type structure (Wyckoff sequence hgf^2e), several ternary examples are listed, however, no distinct structure type for a ternary coloring variant with full atomic ordering was reported.

4. Binary and ternary Laves phases – superstructures

4.1. $MgCu_2$ superstructures

In chapter 3, the coloring variants of Laves phases were described, where the prototype symmetry was kept the same but different atoms fill the individual Wyckoff positions. Given the high space group symmetry, such coloring variants are limited. In many cases a symmetry reduction is required to enable a broader range of ordered compositions and / or small structural distortions. The latter also occur for binaries. The underlying symmetry reductions are discussed on the basis of group-subgroup schemes in the concise and compact Bärnighausen formalism.[93–96] In the main document of this review only the abbreviated Bärnighausen trees are presented; the extended trees for each transition along with the evolution of the atomic parameters are documented in the electronic supplementary information (ESI) file. The basic crystallographic data for selected examples of superstructure representatives of $MgCu_2$ are listed in Table 2.

As a first example we discuss the two modifications of $TbFe_2$.[99,100] The high-temperature (HT) polymorph crystallizes with the cubic $MgCu_2$ type and shows a rhombohedral distortion in going to the low-temperature (LT) regime *via* a *translationengleiche* transition of index 4 (*t*4) from $Fd\bar{3}m$ to $R\bar{3}m$ (Figure 9). This allows for weak distortions that are readily evident in the terbium coordination environment. In the cubic polymorph each terbium atom has regular coordination by twelve iron atoms at 304.6 pm Tb–Fe, while the rhombohedral distortion leads to two crystallographically independent iron sites Fe1 and Fe2 and a small range of Tb–Fe distances between 303.6 to 305.5 pm (Figure 10). Huge magnetostriction and magnetic anisotropy[107,108] are most likely the decisive parameters inducing the structural distortions in $TbFe_2$. We draw back to this phenomenon below, when discussing the $TmNi_2$ structure.

The degree of distortion of the LT-$TbFe_2$ structure can easily be estimated from the *c*/*a* ratio of the unit cell in the hexagonal setting. The ideal value is $\sqrt{2}\times\sqrt{3}\approx 2.449$, while a slightly higher value of 2.471 has been reported for the low-temperature modification.[100] The LT-$TbFe_2$ type (crystallographic fingerprint: space group 166, Pearson code *hR*18 and Wyckoff sequence *dca*) is not a unique case. So far 66 entries are listed in the Pearson database.[31]

The *c*/*a* ratio of the hexagonal cell is the important degree of freedom obtained by the symmetry reduction. While all binaries have *c*/*a* ratios close (slightly larger or smaller) to the ideal $\sqrt{2}\times\sqrt{3}$ ratio, substantial distortions occur for the ternary coloring variants of the LT-$TbFe_2$ type, first observed for Mg_2Ni_3Si.[101] Other prominent representatives are Mg_2Ni_3Ge[64] and the aluminum series RE_2TiAl_3,[109] and the gallides RE_2Rh_3Ga,[110] in total over 30 entries in the Pearson database.[31] A cutout of the Ce_2Rh_3Ga

Table 2. Lattice parameters, space group symbols and unit cell volumes of $MgCu_2$ and the related superstructures and coloring variants.

compound	space group	*a* (pm)	*b* (pm)	*c* (pm)	*V* (nm^3)	*V*/*Z* (nm^3)	Ref.
$MgCu_2$	$Fd\bar{3}m$	699	*a*	*a*	0.3415	0.0427	[3]
$MgCu_4Sn$	$F\bar{4}3m$	704.4	*a*	*a*	0.3495	0.0437	[97]
HT-$TmNi_2$	$P\bar{4}3m$	709.5	*a*	*a*	0.3572	0.0447	[98]
RT-$TmNi_2$	$F\bar{4}3m$	1419.0	*a*	*a*	2.8591	0.0447	[98]
RT-$TbFe_2$	$Fd\bar{3}m$	736.9	*a*	*a*	0.4002	0.0500	[99]
LT-$TbFe_2$	$R\bar{3}m$	518.9(2)	*a*	1282.1(4)	0.2967	0.0495	[100]
Mg_2Ni_3Si	$R\bar{3}m$	500.44(2)	*a*	1108.94(6)	0.2405	0.0401	[101]
RT-YMn_2	$Fd\bar{3}m$	768.0(2)	*a*	*a*	0.4530	0.0566	[102]
LT-YMn_2 (4.2 K)	$F4_1/d12/m$	774.002(7)	*a*	770.009(13)	0.4613	0.0577	[103]
LT-YMn_2 (4.2 K)	$I4_1/amd$	547.3	*a*	770.01	0.2306	0.0577	[103]
RT-HfV_2	$Fd\bar{3}m$	739.7	*a*	*a*	0.4047	0.0506	[104]
LT1-HfV_2 (107.5 K)	$I4_1/amd$	520.71(1)	*a*	740.14(2)	0.2007	0.0502	[105]
LT2-HfV_2 (20 K)	*Imma*	517.35(1)	522.11(1)	743.20(2)	0.2007	0.0502	[105]
Cd_4Cu_7As	*Pnnm*	988.33(7)	712.51(3)	508.95(4)	0.3584	0.0448	[106]

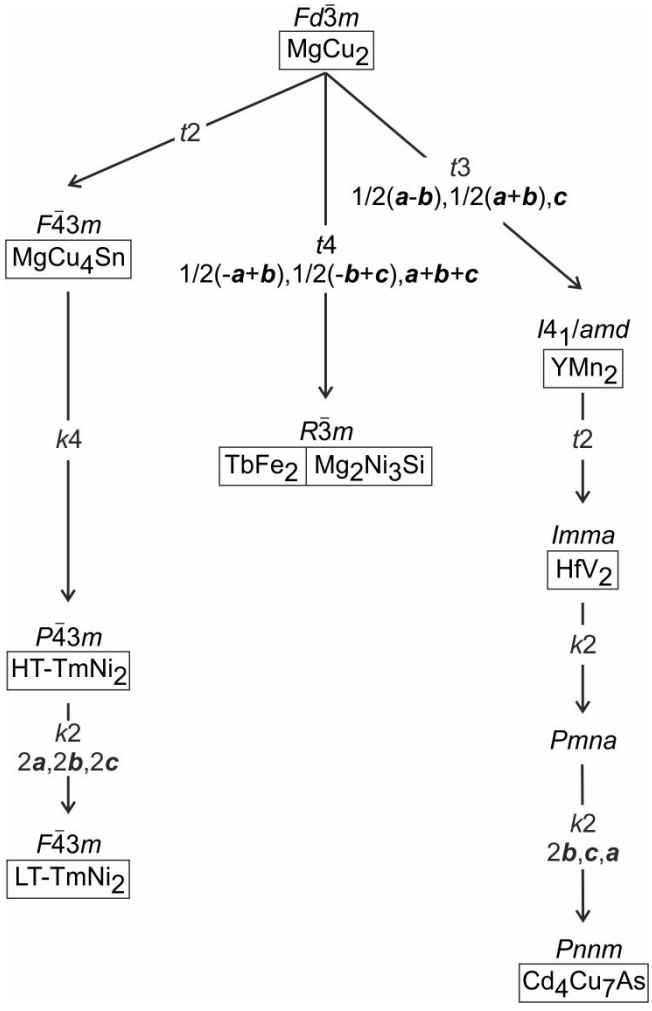

Figure 9. Group-subgroup scheme in the Bärnighausen formalism[93–96] for the $MgCu_2$ superstructures. The indices for the *klassengleiche* (*k*) and *translationengleiche* (*t*) symmetry reductions and the unit cell transformations are given.

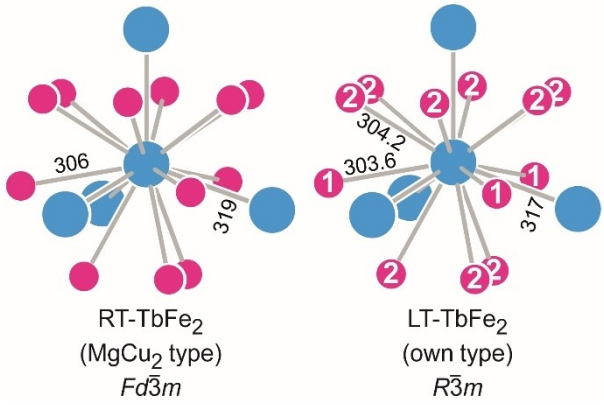

Figure 10. Comparison of the coordination polyhedra around the Tb atoms in RT- (*left*) and LT-$TbFe_2$ (*right*). Interatomic distances are given in pm.

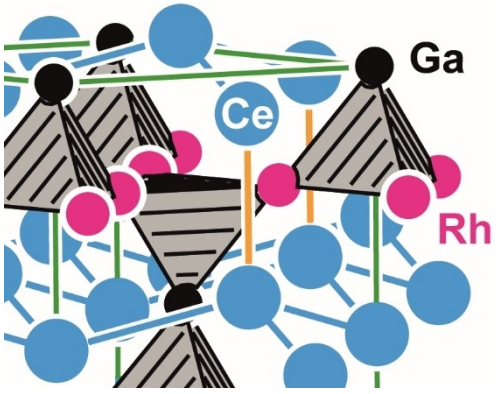

Figure 11. Cutout of the Ce_2Rh_3Ga[110] structure. The short Ce–Ce distances (338 pm) are highlighted in orange.

structure is presented in Figure 11. The symmetry reduction allows for a 3:1 ordering of the transition metal and *p*-element atoms, rhodium and gallium in the present case (Figure S1, ESI). The gallium atoms form the common corners within the networks of condensed tetrahedra. The covalent Rh–Ga bonding along with the differences in size lead to substantially smaller *c*/*a* ratios for

the ternary compounds, i.e. 2.123 for Ce_2Rh_3Ga. It is remarkable, that the *c*/*a* collapse in Ce_2Rh_3Ga is also associated with short Ce–Ce distances of 338 pm, a consequence of almost tetravalent cerium.

The most common (>400 entries in the Pearson database[31]) ordering variant of the cubic Laves phase is the $MgCu_4Sn$ type.[97,111] The coloring occurs for the magnesium substructure of $MgCu_2$. A 1:1 ordering is only possible via a symmetry reduction. In the present case it is the loss of the inversion symmetry ($Fd\bar{3}m \rightarrow F\bar{4}3m$) and the magnesium and tin atoms can order on the 4*a* and 4*c* sites, while the network of condensed copper tetrahedra remains intact (Figure 12). Although the ternary stannide $MgCu_4Sn$ is the prototype for this ordering variant, it is remarkable, that binary Be_5Au[112,113] adopts the same structure with Au on 4*a* and Be on Wyckoff sites 4*c* and 16*e*. This ordering variant is also frequently observed but should be called isopointal to $MgCu_4Sn$ rather than isotypic. So far, more than 170 entries are listed in the Pearson database.[31] The coloring type in $AuBe_5$ leads to two different beryllium coordination patterns, Be1@$Be_{12}Au_4$ and Be2@Be_9Au_3.[114]

The superstructures observed for $TmNi_2$[98] extend the branch of $MgCu_4Sn$ in the Bärnighausen tree discussed above. A *klassengleiche* symmetry reduction of index 4 (*k*4) from $F\bar{4}3m$ to $P\bar{4}3m$ leads to the high-temperature polymorph. LT-$TmNi_2$ then crystallizes in the *klassengleiche* subgroup of index 2 (*k*2), $F\bar{4}3m$, which is finally obtained by doubling the unit cell in all three directions (Figure S2, ESI). The distortions in the LT-$TmNi_2$ structure are small. In total, the subsequent symmetry reductions leads to five crystallographically independent thulium sites in LT-$TmNi_2$. The different coordination polyhedra with relevant interatomic distances are shown in Figure 13. At first sight one might think of a singular example for a complex Laves phase superstructure; however, almost 100 entries are listed in the Pearson database[31] for the LT-$TmNi_2$ type. The small structural distortions observed for $TmNi_2$ might rely on its magnetic ground state. The crystal field parameters derived from temperature dependent susceptibility measurements could be fitted with lower symmetry. The best hint for substantial deviations from cubic symmetry was deduced from ^{169}Tm Mössbauer spectroscopy. The low-temperature spectra show well resolved quadrupolar splitting.[115–119]

The final example for a complex superstructure of the cubic Laves phase concerns the ternary arsenide Cd_4Cu_7As.[106] This is the superstructure with the lowest space group symmetry that deserves four separate steps in the Bärnighausen tree (Figure 9; Figure S3, ESI). In a first *translationengleiche* symmetry reduction to space group $I4_1/amd$ the cubic symmetry is lost. This distortion variant is known as YMn_2 type.[103] A further *translationengleiche* transition of index 2 (*t*2) leads to space group *Imma* where all three lattice parameters are decoupled. This distortion variant exhibits also representatives. It was first observed for HfV_2[105] and there are seven more entries in the Pearson database.[31] Finally, the Cd_4Cu_7As type[106] is then obtained via two further symmetry reduction, a *klassengleiche* transition to space group *Pmna* followed by another *klassengleiche* transition to *Pnnm* upon doubling of the *b* axis. The important point is the splitting of the subcell copper site. In the final space group symmetry, four crystallographically independent sites for atoms of the tetrahedral network are obtained. Only with this last step of symmetry reduction it is possible to allow for a 7:1 ordering. The arsenic atoms occupy the 2*a* site while three Cu sites are observed (8*h*, 4*g* and 2*d*). The Cd_4Cu_7As structure is shown in Figure 14, emphasizing the condensation of Cu_4 and Cu_3As tetrahedra. So far, Cd_4Cu_7As is the sole example for this ordering pattern.

4.2. $MgZn_2$ superstructures

Besides the coloring on the two crystallographically independent zinc sites of the $MgZn_2$ structure (Mg_2Cu_3Si coloring variant, Chapter 3), three different superstructure variants either lead to structural distortions or further coloring varieties. The corresponding Bärnighausen tree for these superstructure variants is shown in Figure 15. Selected examples for superstructures deriving from $MgZn_2$ are summarized in Table 3.

The simplest superstructure concerns $MnCu_4In$,[124] which can be considered as the counterpart compound of $MgCu_4Sn$

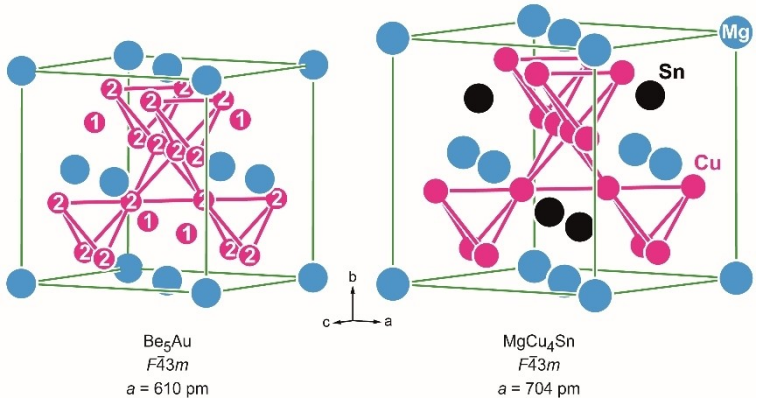

Figure 12. Comparison of the unit cells of Be_5Au (*left*) and $MgCu_4Sn$ (*d*). Au/Mg atoms are shown in blue, Cu/Be atoms in magenta and Sn atoms in black, respectively.

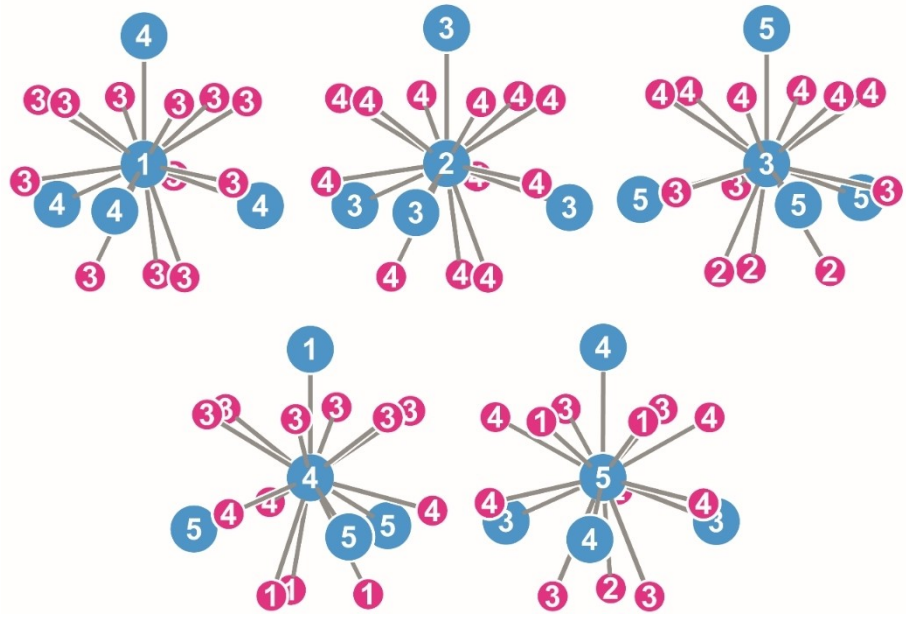

Figure 13. Coordination polyhedra surrounding the five crystallographically independent Tm atoms in the 2×2×2 superstructure of cubic $MgCu_2$ ($F\bar{4}3m$) observed in LT-$TmNi_2$ ($F\bar{4}3m$).

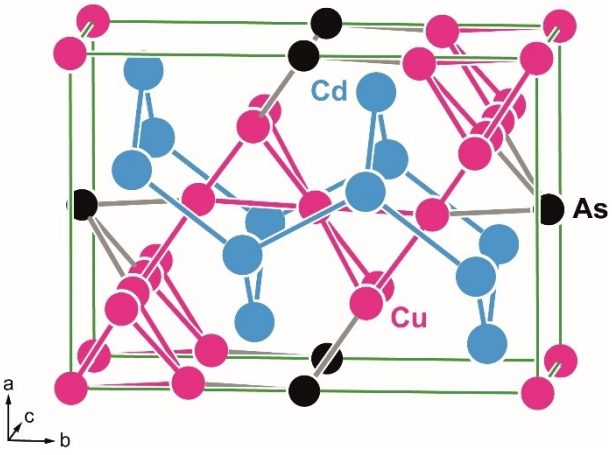

Figure 14. Unit cell of Cd_4Cu_7As (*Pnnm*). Cd, Cu and As atoms are shown as blue, magenta and black spheres, Mg–Mg, Cu–Cu and Cu–As bonds are shown in blue, magenta and grey.

discussed above. Starting from centrosymmetric $MgZn_2$ ($P6_3/mmc$) we lose the inversion symmetry and in the non-centrosymmetric subgroup $P6_3mc$ the Mg site (4*f*) splits into two two-fold sites (2×2*b*) which can then be occupied in an ordered manner by manganese and indium (Figure 16; Figure S4, ESI). This coloring leads only to very small distortions. The ranges of the In–Cu (284.8–291.1 pm) and Mn–Cu (286.4–291.5 pm) are almost similar. It is worthwhile to mention, that the $MnCu_4In$ structure was refined from single crystal X-ray diffractometer data and in parallel by neutron powder diffraction.[124]

The second example of $MgZn_2$ superstructures concerns the substantial orthorhombic distortion in URe_2.[120] This refractory compound crystallizes in the *translationengleiche* subgroup *Cmcm* (Figure 15; Figure S5, ESI). The symmetry reduction leads to a splitting of the Zn2 site (6*h*) and consequently we observe three crystallographically independent rhenium sites (4*a*, 4*c*, 8*g*) in URe_2. Besides this splitting, the decisive distortion is the drastic reduction of the *b*/*a* lattice parameter ratio to 1.514, which considerably deviates from the ideal value of $\sqrt{3} \sim 1.732$.

Table 3. Lattice parameters, space group symbols and unit cell volumes of $MgZn_2$ and the related superstructures and coloring variants.

compound	space group	*a* (pm)	*b* (pm)	*c* (pm)	*V* (nm³)	*V*/*Z* (nm³)	Ref.
$MgZn_2$	$P6_3/mmc$	517	*a*	850	0.1967	0.0492	[5]
Mg_2Cu_3Si	$P6_3/mmc$	500.4	*a*	787.3	0.1707	0.0427	[84]
HT-URe_2 (928 K)	$P6_3/mmc$	540.5(3)	*a*	868.2(3)	0.2197	0.0549	[120]
RT-URe_2	*Cmcm*	560.0(3)	917.8(3)	846.3(3)	0.4350	0.0544	[120]
Mg_2MnGa_3	*Cmcm*	543.2	870.6	858.5	0.4060	0.0508	[121]
$Yb_6Ir_5Ga_7$	$P6_3/mcm$	930.4(1)	*a*	843.1(1)	0.6320	0.3160	[122]
$Nb_{6.4}Ir_4Al_{7.4}$	$P6_3/mcm$	884.0	*a*	822.0	0.5563	0.2782	[123]
$MnCu_4In$	$P6_3mc$	497.08(4)	*a*	794.0(1)	0.1699	0.0850	[124]

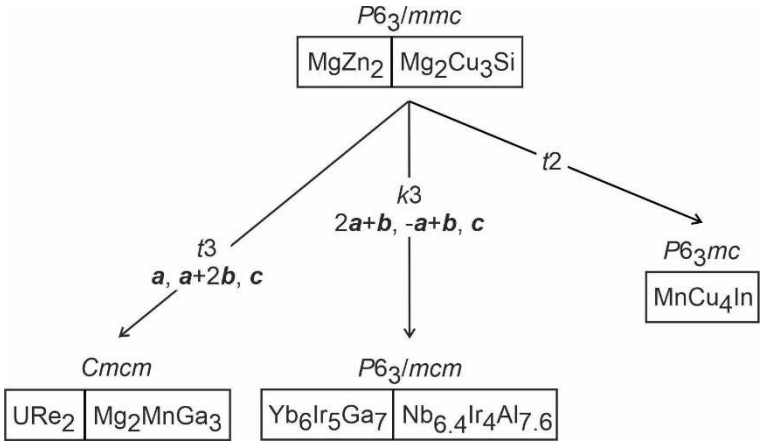

Figure 15. Group-subgroup scheme for $MgZn_2/Mg_2Cu_3Si$ superstructures in the Bärnighausen formalism.[93–96] The indices for the *klassengleiche* (*k*) and *translationengleiche* (*t*) symmetry reductions and the unit cell transformations are given.

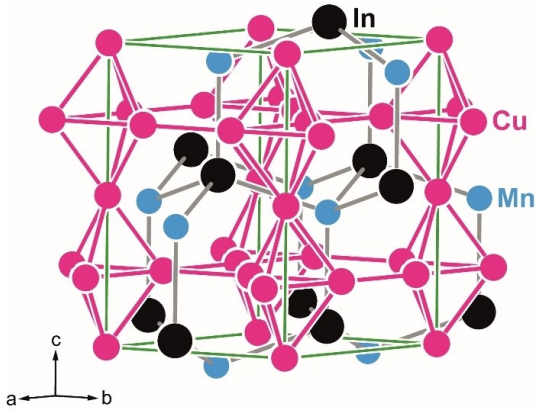

Figure 16. Unit cell of $MnCu_4In$ ($P6_3mc$). Mn, Cu and In atoms are shown as blue, magenta and black spheres, Cu–Cu and Mn–In bonds are shown in magenta and grey.

Since URe_2 is dimorphic with a $MgZn_2$ type high-temperature polymorph, it is interesting to compare the uranium coordination in both modifications (Figure 17). In HT-URe_2 the uranium atoms are coordinated by twelve rhenium atoms with U–Re distances ranging from 312.8 to 316.8 pm. The strongly distorted low-temperature modification shows eight nearest rhenium neighbors around uranium (300.7–313.2 pm), while four further neighbors show longer U–Re distances of 322.9 and 324.4 pm, pointing to an 8 + 4 coordination. The reason for the substantial orthorhombic distortion of the URe_2 structure is not easy to understand. The physical properties give no pronounced hint since URe_2 shows an essentially temperature-independent, slightly positive magnetic susceptibility, indicative of Pauli paramagnetism.[125]

Similar to $MgZn_2$, also the orthorhombically distorted superstructure has a coloring variant. It was recently reported for the gallide Mg_2MnGa_3,[121] where two of the rhenium sites are occupied by gallium and one by manganese. The manganese-gallium coloring (i.e. the difference in size between these two elements) leads to a reduction of the *b*/*a* lattice parameter ratio 1.601, similar to URe_2 discussed above. It is interesting to note, that the inverse coloring has been observed for the stannide Eu_2Pd_3Sn and the isotypic compounds Sr_2Pd_3Sn and Eu_2Pd_3In.[126] The coloring variants of both compounds are

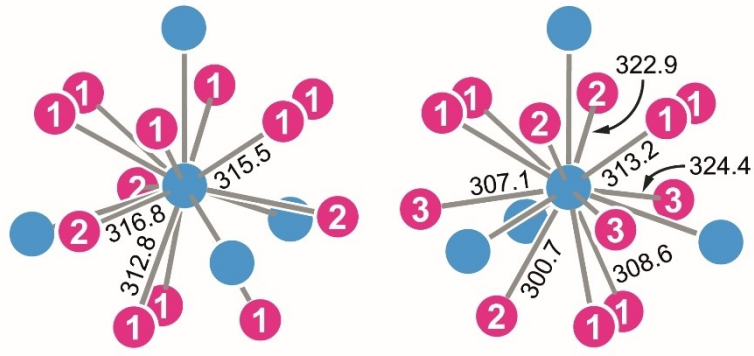

Figure 17. Coordination polyhedra surrounding the U atoms in (*left*) HT-URe_2 ($MgZn_2$ type, $P6_3/mmc$) and (*right*) LT-URe_2 (own type, *Cmcm*).

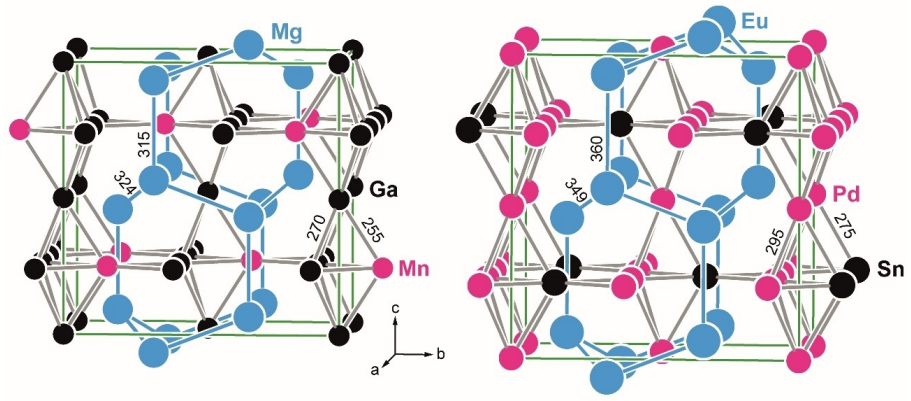

Figure 18. Unit cells of (*left*) Mg_2MnGa_3 and (*right*) Eu_2Pd_3Sn (both *Cmcm*) showing an inverse coloring of the polyanionic network. Interatomic distances are given in pm. Mg/Eu, Mn/Pd and Ga/Sn are drawn in blue, magenta and black, respectively.

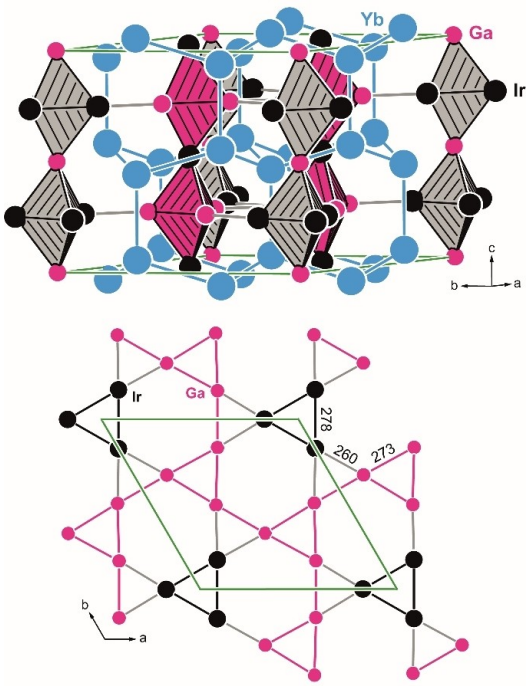

Figure 19. (*top*) Unit cell of $Yb_6Ir_5Ga_7$. The two rows of ordered tetrahedra $IrGa_3$ (grey) and Ir_3Ga (magenta) are highlighted. (*bottom*) kagome net in the structure of $Yb_6Ir_5Ga_7$. Interatomic distances are given in pm.

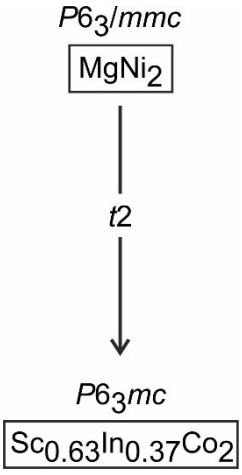

Figure 20. Group-subgroup scheme in the Bärnighausen formalism[93–96] for the $MgNi_2$ superstructure $Sc_{0.63}In_{0.37}Co_2$.[128] The index for the *translationengleiche* (*t*) symmetry reduction is given.

shown in Figure 18. The distortion in Eu_2Pd_3Sn ($b/a = 1.557$) is stronger than in the gallide.

The last example of a $MgZn_2$ superstructure deals with the Al-compound $Nb_{6.4}Ir_4Al_{7.6}$.[123] This superstructure variant was already reported by Horyń in 1977. The symmetry reduction proceeds via a *klassengleiche* transition of index 3 (*k*3) from $P6_3/mmc$ to $P6_3/mcm$ (Figure 15; Figure S6, ESI). The cell enlargement was correctly assigned; however, the structure model still shows mixed occupied sites, similar to $V_6Co_{6.84}Si_{5.16}$[14] and $Mg_6Ni_{7.8}Ge_{4.2}$.[64] $Yb_6Ir_5Ga_7$[122] was the first example of that superstructure variant with a complete ordering on the tetrahedral substructure. This was meanwhile also observed for the rare earth-based series $RE_6Ir_5Ga_7$[127] and $RE_6T_5Al_7$ (T = Ru, Ir).[92] The reason for superstructure formation is the different coloring within the rows of face- and corner-sharing tetrahedra. For $Yb_6Ir_5Ga_7$ we observe rows of condensed $IrGa_3$ and Ir_3Ga tetrahedra in 2:1 ratio, leading to the $[Ir_5Ga_7]$ substructure (Figure 19). The size of iridium and gallium is different. In order to have the same translation period for both rows of condensed tetrahedra, the triangles of the Ga2 and Ir2 atoms have free *x* parameters for adjusting geometrical requests, leading to smaller and larger triangles within the kagome network (Figure 19).

It is worthwhile to note that the Pearson data base lists more than 2000 entries for the structure type $MgZn_2$. Besides the pure binaries phases, many ternaries and even extended solid solutions have been reported, many close to an equiatomic composition. It is likely, that at least some of these phases might adopt the $Yb_6Ir_5Ga_7$ type coloring variant.

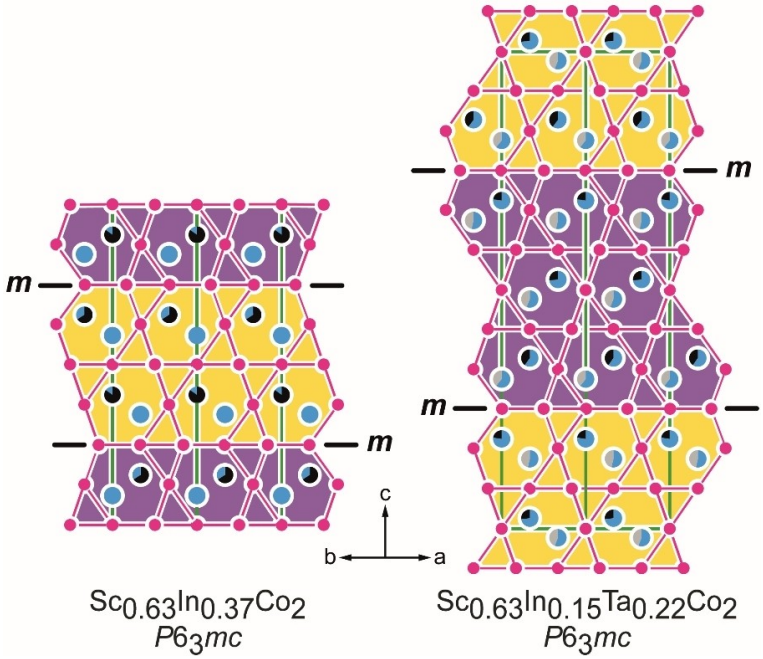

Figure 21. Projections of the unit cells of the Laves phases $Sc_{0.63}In_{0.37}Co_2$ (*left*) and $Sc_{0.63}In_{0.15}Ta_{0.22}Co_2$ (*right*). The transition metal networks formed by the Co atoms are drawn in magenta, the Sc atoms in blue, In is drawn in black and Ta in grey. The respective mixing is indicated by the segmented circles. The blocks that derive from the $MgCu_2$ type are shaded in yellow, their mirrored versions in purple. The mirror planes (*m*) related with the chemical twinning are indicated. The unit cell edges are shown in green; the space groups are given.

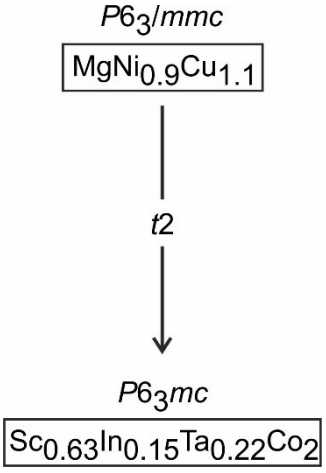

Figure 22. Group-subgroup scheme in the Bärnighausen formalism[93–96] for the $MgNi_{0.9}Cu_{1.1}$ superstructure $Sc_{0.63}In_{0.15}Ta_{0.22}Co_2$. The index for the *translationengleiche* (*t*) symmetry reduction is given.

4.3. Superstructures of $MgNi_2$ and $MgNi_{0.9}Cu_{1.1}$

The third well-known member of the binary Laves phases is $MgNi_2$. As described in Chapter 2, we can easily describe the $MgNi_2$ structure via chemical twinning of the basic slab of $MgCu_2$. Substitution on the magnesium sites can force superstructure formation. This is the case for $Sc_{0.63}In_{0.37}Co_2$.[128] The scandium-indium coloring along with different site occupancies leads to a loss of the mirror plane that we discussed for the chemical twinning. $Sc_{0.63}In_{0.37}Co_2$ shows a simple *translationengleiche* symmetry reduction from $P6_3/mmc$ to $P6_3mc$ (Figure 20; Figure S7, ESI). This is readily evident from the projection perpendicular to the kagome nets in Figure 21.

$Sc_{0.63}In_{0.15}Ta_{0.22}Co_2$[129] shows exactly the same pattern of superstructure formation as $Sc_{0.63}In_{0.37}Co_2$.[128] The only difference concerns the width of the building blocks, i.e. two subsequent $MgCu_2$ slabs in $Sc_{0.63}In_{0.37}Co_2$ but three in $Sc_{0.63}In_{0.15}Ta_{0.22}Co_2$. The loss of inversion symmetry (Figure 22; Figure S8, ESI) is driven by the different Sc/In respectively Sc/Ta occupancies as emphasized in Figure 21.

5. Conclusion

The present review focusses on the structural chemistry and superstructures of Laves phases. As shown, many coloring and distortion variants have been reported, also in recent years indicating that Laves phases are still an interesting field of research. Not all reasons for the observed distortion are known, however, the stabilization of certain bonding situations can be assumed to be the major reasons. Coloring of the Laves phases are simpler to understand since here only atoms in an existing structure are exchanged while superstructure formations are more complex.

Author contribution

All authors have accepted responsibility for the entire content of this submitted manuscript and approved the submission.

Acknowledgements

Funding is provided by the Deutsche Forschungsgemeinschaft DFG (JA 1891-10-1). Open Access funding enabled and organized by Projekt DEAL.

Conflict of Interest

The authors declare no conflicts of interest regarding this article.

Keywords: Intermetallic structures · Laves phases · Superstructures · Group-subgroup schemes

[1] W. Fischer, *Z. Kristallogr.* **2006**, *221*, 305–310.
[2] E. Parthé, *Z. Kristallogr.* **2006**, *221*, 301–304.
[3] J. B. Friauf, *J. Am. Chem. Soc.* **1927**, *49*, 3107–3114.
[4] J. B. Friauf, *Phys. Rev.* **1927**, *29*, 34–40.
[5] L. Tarschisch, A. T. Titow, F. K. Garjanow, *Phys. Z. Sowjetunion* **1934**, *5*, 503–510.
[6] F. Laves, H. Witte, *Metallwirtsch.* **1935**, *14*, 645–649.
[7] K. H. Lieser, H. Witte, *Z. Metallkd.* **1952**, *43*, 396–401.
[8] F. Laves, H. Witte, *Metallwirtsch.* **1936**, *15*, 840–842.
[9] G. E. R. Schulze, *Z. Elektrochem. Angew. Phys. Chem.* **1939**, *45*, 849–865.
[10] P. Paufler, *Z. Kristallogr.* **2006**, *221*, 311–318.
[11] K. A. Gschneidner Jr, V. K. Pecharsky, *Z. Kristallogr.* **2006**, *221*, 375–381.
[12] T. Yokosawa, K. Söderberg, M. Boström, D. Grüner, G. Kreiner, O. Terasaki, *Z. Kristallogr.* **2006**, *221*, 357–374.
[13] D. Grüner, F. Stein, M. Palm, J. Konrad, A. Ormeci, W. Schnelle, Y. Grin, G. Kreiner, *Z. Kristallogr.* **2006**, *221*, 319–333.
[14] M. Conrad, C. Pohling, H. Webert, B. Harbrecht, *Z. Kristallogr.* **2006**, *221*, 349–356.
[15] A. Grytsiv, X.-Q. Chen, V. T. Witusiewicz, P. Rogl, R. Podloucky, V. Pomjakushin, D. Maccio, A. Saccone, G. Giester, F. Sommer, *Z. Kristallogr.* **2006**, *221*, 334–348.
[16] A. Ormeci, A. Simon, Y. Grin, *Angew. Chem. Int. Ed.* **2010**, *49*, 8997–9001.
[17] R. L. Johnston, R. Hoffmann, *Z. Anorg. Allg. Chem.* **1992**, *616*, 105–120.
[18] R. Nesper, *Angew. Chem.* **1991**, *103*, 805–834.
[19] R. Nesper, *Angew. Chem. Int. Ed.* **1991**, *30*, 789–817.
[20] F. Stein, M. Palm, G. Sauthoff, *Intermetallics* **2004**, *12*, 713–720.
[21] F. Stein, M. Palm, G. Sauthoff, *Intermetallics* **2005**, *13*, 1056–1074.
[22] F. Stein, A. Leineweber, *J. Mater. Sci.* **2021**, *56*, 5321–5427.
[23] K. A. Gschneidner Jr, V. K. Pecharsky, A. O. Tsokol, *Rep. Prog. Phys.* **2005**, *68*, 1479.
[24] S. F. Matar, *Prog. Solid State Chem.* **2010**, *38*, 1–37.
[25] V. A. Yartys, M. V. Lototskyy, *J. Alloys Compd.* **2022**, *916*, 165219.
[26] K.-H. Young, S. Chang, X. Lin, *Batteries* **2017**, *3*, 27.
[27] R. Demchyna, S. Leoni, H. Rosner, U. Schwarz, *Z. Kristallogr.* **2006**, *221*, 420–434.
[28] E. Parthé, *Elements of inorganic structural chemistry - a course on selected topics*, K. Sutter Parthé, Petit-Lancy, Switzerland, **1990**.
[29] E. Parthé, *Elements of inorganic structural chemistry - selected efforts to predict structural features*, K. Sutter Parthé, Petit-Lancy, Switzerland, **1996**.
[30] R. Pöttgen, *Z. Anorg. Allg. Chem.* **2014**, *640*, 869–891.
[31] P. Villars, K. Cenzual, *Pearson's Crystal Data: Crystal Structure Database for Inorganic Compounds*, ASM International®, Materials Park, Ohio, USA **2023**.
[32] K. D. Dorfman, *Macromolecules* **2021**, *54*, 10251–10270.
[33] C. M. Baez-Cotto, M. K. Mahanthappa, *ACS Nano* **2018**, *12*, 3226–3234.
[34] H. Fukui, N. Hirao, Y. Ohishi, A. Q. R. Baron, *J. Phys.: Condens. Matter* **2010**, *22*, 095401.
[35] C. Ji, A. F. Goncharov, V. Shukla, N. K. Jena, D. Popov, B. Li, J. Wang, Y. Meng, V. B. Prakapenka, J. S. Smith, R. Ahuja, W. Yang, H.-k. Mao, *Proc. Nat. Acad. Sci.* **2017**, *114*, 3596–3600.
[36] D. Laniel, G. Weck, P. Loubeyre, *Phys. Rev. B* **2016**, *94*, 174109.
[37] R. Nesper, G. J. Miller, *J. Alloys Compd.* **1993**, *197*, 109–121.
[38] J. H. Zhu, P. K. Liaw, C. T. Liu, *Mater. Sci. Eng. A* **1997**, *239–240*, 260–264.
[39] C. T. Liu, J. H. Zhu, M. P. Brady, C. G. McKamey, L. M. Pike, *Intermetallics* **2000**, *8*, 1119–1129.
[40] F. C. Frank, J. S. Kasper, *Acta Crystallogr.* **1959**, *12*, 483–499.
[41] F. Laves, *Z. Kristallogr.* **1931**, *78*, 208–241.
[42] S. Samson, *Structural Principles of Giant Cellsin Developments in the Structural Chemistry of Alloy Phases: Based on a symposium sponsored by the Committee on Alloy Phases of the Institute of Metals Division, the Metallurgical Society, American Institute of Mining, Metallurgical and Petroleum Engineers, Cleveland, Ohio, October, 1967*, Ed.: B. C. Giessen, Springer US, Boston, MA, **1969**, p. 65–106.
[43] L. S. Ramsdell, *Am. Mineral.* **1947**, *32*, 64–82.
[44] S. Andersson, B. G. Hyde, *J. Solid State Chem.* **1974**, *9*, 92–101.
[45] S. Andersson, *Angew. Chem. Int. Ed.* **1983**, *22*, 69–81.
[46] E. Parthé, B. Chabot, K. Cenzual, *Chimia* **1985**, *39*, 164–174.
[47] Y. Komura, *Acta Crystallogr.* **1962**, *15*, 770–778.
[48] Y. Komura, E. Kishida, M. Inoue, *J. Phys. Soc. Jpn.* **1967**, *23*, 398–404.
[49] Y. Komura, M. Mitarai, I. Nakatani, H. Iba, T. Shimizu, *Acta Crystallogr.* **1970**, *B26*, 666–668.
[50] Y. Komura, M. Mitarai, A. Nakaue, S. Tsujimoto, *Acta Crystallogr.* **1972**, *B28*, 976–978.
[51] Y. Komura, A. Nakaue, M. Mitarai, *Acta Crystallogr.* **1972**, *B28*, 727–732.
[52] Y. Komura, Y. Kitano, *Acta Crystallogr.* **1977**, *B33*, 2496–2501.
[53] Y. Kitano, Y. Komura, H. Kajiwara, E. Watanabe, *Acta Crystallogr.* **1980**, *A36*, 16–21.
[54] Y. Komura, K. Tokunaga, *Acta Crystallogr.* **1980**, *B36*, 1548–1554.
[55] Y. Komura, Y. Kitano, *Acta Crystallogr.* **1977**, *B33*, 2496–2501.
[56] Y. Kitano, Y. Komura, H. Kajiwara, *Trans. Jpn. Inst. Met.* **1977**, *18*, 39–45.
[57] R. Haydock, R. L. Johannes, *J. Phys. F: Metal Phys.* **1975**, *5*, 2055.
[58] Y. Ohta, D. G. Pettifor, *J. Phys. Condens. Matter* **1990**, *2*, 8189.
[59] Y. Kubota, M. Takata, M. Sakata, T. Ohba, K. Kifune, T. Tadaki, *J. Phys.: Condens. Matter* **2000**, *12*, 1253.
[60] W. Chen, J. Sun, *Physica B + C* **2006**, *382*, 279–284.
[61] D. Grüner, *Untersuchungen zur Natur der Laves-Phasen in Systemen der Übergangsmetalle*, Dissertation, Technischen Universität Dresden, Dresden, **2007**.
[62] C.-w. Zhang, *Physica B + C* **2008**, *403*, 2088–2092.

[63] W. Steurer, J. Dshemuchadse, *Intermetallics*, Union of Crystallography, Oxford University Press, Oxford, **2016**.
[64] L. Siggelkow, V. Hlukhyy, T. F. Fässler, *Z. Anorg. Allg. Chem.* **2017**, *643*, 1424–1430.
[65] J. Bodega, J. F. Fernández, F. Leardini, J. R. Ares, C. Sánchez, *J. Phys. Chem. Solids* **2011**, *72*, 1334–1342.
[66] P. A. Farrer, H. Margolin, *Trans. Metall. Soc. AIME* **1963**, *227*, 1342–1346.
[67] V. N. Svechnikov, M. Y. Teslyuk, Y. A. Kocherzhinskii, V. V. Pet'kov, E. V. Dabizha, *Dopov. Akad. Nauk Ukr. RSR Ser. A* **1970**, 837–840.
[68] J. R. Johnson, J. J. Reilly, *Inorg. Chem.* **1978**, *17*, 3103–3108.
[69] W. Baumann, A. Leineweber, *J. Alloys Compd.* **2010**, *505*, 492–496.
[70] M. Coduri, S. Mauri, C. A. Biffi, A. Tuissi, *Intermetallics* **2019**, *109*, 110–122.
[71] K. S. Kumar, P. M. Hazzledine, *Intermetallics* **2004**, *12*, 763–770.
[72] P. M. Hazzledine, P. Pirouz, *Scr. Metall. Mater.* **1993**, *28*, 1277–1282.
[73] H. Nowotny, E. Wormnes, A. Mohrnheim, *Z. Metallkd.* **1940**, *32*, 39–42.
[74] G. Nagorsen, H. Posch, H. Schäfer, A. Weiss, *Z. Naturforsch.* **1969**, *24b*, 1191.
[75] E. J. Duwell, N. C. Baenziger, *Acta Crystallogr.* **1955**, *8*, 705–710.
[76] M. L. Fornasini, G. Bruzzone, *J. Less-Common Met.* **1975**, *40*, 335–340.
[77] G. Bruzzone, F. Merlo, *J. Less-Common Met.* **1975**, *39*, 1–6.
[78] S. Amerioun, T. Yokosawa, S. Lidin, U. Häussermann, *Inorg. Chem.* **2004**, *43*, 4751–4760.
[79] G. Cordier, E. Czech, H. Schäfer, *Z. Naturforsch.* **1982**, *37b*, 1442–1445.
[80] G. Cordier, E. Czech, H. Schäfer, *Z. Naturforsch.* **1984**, *39b*, 421–423.
[81] S. Kal, E. Stoyanov, J.-P. Belieres, T. L. Groy, R. Norrestam, U. Häussermann, *J. Solid State Chem.* **2008**, *181*, 3016–3023.
[82] S. Engel, E. C. J. Gießelmann, L. E. Schank, G. Heymann, K. Brix, R. Kautenburger, H. P. Beck, O. Janka, *Inorg. Chem.* **2023**, *62*, 4260–4271.
[83] H. Witte, *Metallwirtsch. Metallwiss. Metalltech.* **1939**, *18*, 459–463.
[84] H. Witte, *Z. Angew. Mineral.* **1938**, *1*, 255–268.
[85] T. Mishra, R.-D. Hoffmann, C. Schwickert, R. Pöttgen, *Z. Naturforsch.* **2011**, *66b*, 771–776.
[86] F. Eustermann, F. Stegemann, S. Gausebeck, O. Janka, *Z. Naturforsch.* **2018**, *73b*, 819–830.
[87] X. L. Yan, X.-Q. Chen, A. Grytsiv, V. T. Witusiewicz, P. Rogl, R. Podloucky, G. Giester, *J. Alloys Compd.* **2007**, *429*, 10–18.
[88] H. Oesterreicher, *J. Less-Common Met.* **1971**, *25*, 341–342.
[89] H. Oesterreicher, *J. Appl. Phys.* **1971**, *42*, 5137–5143.
[90] H. Oesterreicher, *J. Less-Common Met.* **1971**, *25*, 228–230.
[91] A. V. Morozkin, V. K. Genchel, A. V. Garshev, V. O. Yapaskurt, R. Nirmala, S. Quezado, S. K. Malik, *J. Solid State Chem.* **2017**, *253*, 238–241.
[92] F. Eustermann, F. Stegemann, M. Radzieowski, O. Janka, *Inorg. Chem.* **2019**, *58*, 16211–16226.
[93] H. Bärnighausen, *MATCH, Commun. Math. Comput. Chem.* **1980**, *9*, 139–175.
[94] U. Müller, *Z. Anorg. Allg. Chem.* **2004**, *630*, 1519–1537.
[95] H. Wondratschek, U. Müller, *International Tables for Crystallography, Volume A1: Symmetry relations between space groups*, John Wiley & Sons, Chichester, Großbritannien, **2011**.
[96] U. Müller, *Symmetry Relationships between Crystal Structures*, Oxford University Press, **2013**.
[97] E. I. Gladyshevskii, P. I. Krypyakevych, M. Y. Teslyuk, *Dokl. Akad. Nauk SSSR* **1952**, *85*, 81–84.
[98] A. F. Deutz, R. B. Helmholdt, A. C. Moleman, D. B. De Mooij, K. H. J. Buschow, *J. Less-Common Met.* **1989**, *153*, 259–266.
[99] P. I. Krypyakevych, M. Y. Teslyuk, D. P. Frankevich, *Sov. Phys. Crystallogr.* **1965**, *10*, 422–423.
[100] A. E. Dwight, C. W. Kimball, *Acta Crystallogr.* **1974**, *B30*, 2791–2793.
[101] D. Noréus, L. Eriksson, L. Göthe, P. E. Werner, *J. Less-Common Met.* **1985**, *107*, 345–349.
[102] B. J. Beaudry, J. F. Haefling, A. H. Daane, *Acta Crystallogr.* **1960**, *13*, 743–744.
[103] R. Cywinski, S. H. Kilcoyne, C. A. Scott, *J. Phys.: Condens. Matter* **1991**, *3*, 6473.
[104] R. P. Elliott, W. Rostoker, *Trans. Am. Soc. Met.* **1958**, *50*, 617–633.
[105] Y. Zhao, F. Chu, R. B. Von Dreele, Q. Zhu, *Acta Crystallogr.* **2000**, *B56*, 601–606.
[106] O. Osters, T. Nilges, M. Schöneich, P. Schmidt, J. Rothballer, F. Pielnhofer, R. Weihrich, *Inorg. Chem.* **2012**, *51*, 8119–8127.
[107] A. E. Clark, *AIP Conf. Proc.* **1974**, *18*, 1015–1029.
[108] W. M. d. Azevedo, I. S. Mackenzie, Y. Berthier, *J. Phys. F: Metal Phys.* **1985**, *15*, L243–L246.
[109] E. C. J. Gießelmann, S. Engel, I. El Saudi, L. Schumacher, M. Radieowski, J. M. Gerdes, O. Janka, *Solids* **2023**, accepted.
[110] S. Seidel, O. Janka, C. Benndorf, B. Mausolf, F. Haarmann, H. Eckert, L. Heletta, R. Pöttgen, *Z. Naturforsch.* **2017**, *72b*, 289–303.
[111] K. Osamura, Y. Murakami, *J. Less-Common Met.* **1978**, *60*, 311–313.
[112] L. Misch, *Metallwirtsch. Metallwiss. Metalltech.* **1935**, *14*, 897–899.
[113] S. S. Sidhu, C. O. Henry, *J. Appl. Phys.* **1950**, *21*, 1036–1037.
[114] O. Janka, R. Pöttgen, *Z. Naturforsch.* **2020**, *75b*, 421–439.
[115] J. Farrell, W. E. Wallace, *Inorg. Chem.* **1966**, *5*, 105–109.
[116] R. Abbundi, A. Clark, O. McMasters, *IEEE Trans. Magn.* **1980**, *16*, 1074–1076.
[117] M. R. Ibarra, J. I. Arnaudas, P. A. Algarabel, A. del Moral, *J. Magn. Magn. Mater.* **1984**, *46*, 167–177.
[118] P. C. M. Gubbens, A. M. v. d. Kraan, K. H. J. Buschow, *J. Phys. F: Metal Phys.* **1984**, *14*, 2195.
[119] A. F. Deutz, H. B. Brom, C. D. Wentworth, W. J. Huiskamp, L. J. de Jongh, K. H. J. Buschow, *J. Magn. Magn. Mater.* **1989**, *78*, 176–182.
[120] B. Hatt, *Acta Crystallogr.* **1961**, *14*, 119–123.
[121] I. V. Chumak, V. V. Pavlyuk, V. H. Hlukhyy, R. Pöttgen, *Abstr. 9th Int. Conf. Crystal Chem. Intermet. Compd.* **2005**, 83.
[122] S. Seidel, R. Pöttgen, *Z. Anorg. Allg. Chem.* **2017**, *643*, 261–265.
[123] R. Horyń, *J. Less-Common Met.* **1977**, *56*, 103–111.
[124] A. Provino, D. Paudyal, M. L. Fornasini, I. Dhiman, S. K. Dhar, A. Das, Y. Mudryk, P. Manfrinetti, V. K. Pecharsky, *Acta Mater.* **2013**, *61*, 2236–2243.
[125] M. B. Brodsky, R. J. Trainor, A. T. Aldred, C. H. Sowers, *J. Appl. Phys.* **2008**, *49*, 1498–1499.
[126] J. Wiethölter, A. Koldemir, T. Block, M. K. Reimann, S. Klenner, R. Pöttgen, *Z. Kristallogr.* **2023**, *238*, 201–208.
[127] F. Eustermann, A. Pominov, R. Pöttgen, *Z. Anorg. Allg. Chem.* **2018**, *644*, 1297–1303.
[128] N. L. Gulay, Y. M. Kalychak, R. Pöttgen, *Z. Anorg. Allg. Chem.* **2021**, *647*, 75–80.
[129] N. L. Gulay, Y. M. Kalychak, R. Pöttgen, *Z. Naturforsch.* **2021**, *76b*, 345–354.

Manuscript received: May 23, 2023
Accepted manuscript online: June 18, 2023

